Thermal stability of Te-hyperdoped Si: Atomic-scale correlation of the structural, electrical, and optical properties

Mao Wang,[1,2,*] R. Hübner,[1] Chi Xu,[1,2] Yufang Xie,[1,2] Y. Berencén,[1] R. Heller,[1] L. Rebohle,[1] M. Helm,[1,2] S. Prucnal,[1] and Shengqiang Zhou[1]

[1]*Helmholtz-Zentrum Dresden-Rossendorf, Institute of Ion Beam Physics and Materials Research, Bautzner Landstrasse 400, 01328 Dresden, Germany*

[2]*Technische Universität Dresden, 01062 Dresden, Germany*

(Received 4 January 2019; published 26 April 2019)

Si hyperdoped with chalcogens (S,Se,Te) is well known to possess unique properties such as an insulator-to-metal transition and a room-temperature sub-band-gap absorption. These properties are expected to be sensitive to a postsynthesis thermal annealing, since hyperdoped Si is a thermodynamically metastable material. Thermal stability of the as-fabricated hyperdoped Si is of great importance for the device fabrication process involving temperature-dependent steps such as Ohmic contact formation. Here, we report on the thermal stability of the as-fabricated Te-hyperdoped Si subjected to isochronal furnace anneals from 250 to 1200 °C. We demonstrate that Te-hyperdoped Si exhibits thermal stability up to 400 °C for 10 min, which even helps to further improve the crystalline quality, the electrical activation of Te dopants, and the room-temperature sub-band-gap absorption. At higher temperatures, however, Te atoms are found to move out from the substitutional sites with a maximum migration energy of $E_M = 2.3$ eV forming inactive clusters and precipitates that impair the structural, electrical, and optical properties. These results provide further insight into the underlying physical state transformation of Te dopants in a metastable compositional regime caused by postsynthesis thermal annealing. They also pave the way for the fabrication of advanced hyperdoped Si-based devices.

DOI: 10.1103/PhysRevMaterials.3.044606

I. INTRODUCTION

The nonequilibrium method of ion implantation followed by nanosecond-pulsed laser melting (PLM) is extensively used for doping silicon with impurity concentrations several orders of magnitude above the solid solubility limit (hyperdoping) [1–3]. Such a hyperdoping approach has attracted interest for decades due to the possibility of designing Si with unique and exotic physical properties. In the microelectronic industry, Si hyperdoped with shallow-level impurities such as As (or P, B, or Sb) allows for the formation of shallow junctions with high electrical conductivity [3–5]. Recently, it has been shown that Si hyperdoped with deep-level (with a much higher ionization energy) impurities (Ti, Ag, Au, S, Se, and Te) exhibits strong sub-band-gap absorption caused by the presence of an intermediate band within the band gap of Si. This finding is a major step toward the implementation of room-temperature broadband infrared photodetectors [6–14] and high-efficiency solar cells [15–20]. Moreover, hyperdoped Si provides a good prospect to explore the impurity-mediated insulator-to-metal transition (IMT) in Si [21–25].

However, it should be noted that hyperdoped Si is a metastable and supersaturated solid solution system. The novel physical properties mentioned above are expected to be strongly altered by a subsequent thermal treatment [26–31]. Therefore, a comprehensive study regarding subsequent thermal treatments is of great interest not only for the nature of thermal deactivation, but also for the thermal stability of the necessary subsequent processes to produce the ultimate devices by complementary-metal-oxide-semiconductor (CMOS)-compatible processing. Previous investigations on hyperdoped Si with shallow-level dopants suggested that the main mechanism behind the thermally unstable deactivation is the formation of defect complexes (dopant-vacancy clusters) and precipitates depending on the thermal anneals [30,32,33]. The thermal deactivation of sub-band-gap absorption in hyperdoped Si with deep-level impurities is attributed to the long-range dopants diffusion (in polycrystalline Si) or to the formation of dopant-defect complexes (in single-crystalline Si) [29,31]. However, a direct correlation between the impurity lattice location and the electrical and optical properties upon thermal annealing has not been established yet.

In this work, we explore the thermal stability of an epitaxial Te-hyperdoped Si layer by using furnace annealing in the temperature range of 250–1200 °C. We demonstrate that the as-fabricated Te-hyperdoped Si layers are thermally stable upon annealing for 10 min up to 400 °C. In particular, the crystalline quality, the Te substitutionality, the electrical activation, and the midinfrared absorption slightly improve, which is crucial for producing CMOS-compatible devices. Moreover, we show that the deactivation process at annealing temperatures higher than 500 °C results from the thermally mediated atomic movements of Te dopants to form inactive complexes or precipitates in the metastable hyperdoped system. This finding provides further insight into the underlying

*Author to whom all correspondence should be addressed: m.wang@hzdr.de

physical state transformation of Te dopants in a metastable compositional regime caused by thermal treatment.

II. METHODS

A. Sample preparation

Two kinds of (100) Si wafers were used for the ion implantation process: (a) a single-side polished intrinsic Si wafer ($\rho > 10^4\,\Omega\,\mathrm{cm}$) for structural and electrical characterization, and (b) a double-side polished *p*-type Si wafer (boron-doped, $\rho \approx 1-10\,\Omega\,\mathrm{cm}$) for the investigation of the optical properties. Both the implantation and the annealing conditions were always identical. Samples were prepared by a combined implantation of Te ions with implantation energies of 150 and 50 keV (to obtain a homogeneous distribution of Te in the implanted layer) at room temperature to a dose of 4.7×10^{15} and $1.9 \times 10^{15}\,\mathrm{cm}^{-2}$, respectively. Samples were tilted by $\sim 7^\circ$ off the incident beam to minimize the channeling effect. Based on the previous Rutherford backscattering-channeling spectrometry (RBS/C) measurements and transmission electron microscopy (TEM) results [12], the implanted layer has a thickness of 120 nm with a peak Te concentration of $7.5 \times 10^{20}\,\mathrm{cm}^{-3}$. The ion-implanted samples were subsequently irradiated in air with one pulse by a spatially homogenized, pulsed XeCl excimer laser (Coherent COMPexPRO201, wavelength of 308 nm, pulse duration of 28 ns) with a square spot of approximately 5 mm × 5 mm [12]. At this laser density, the Te-implanted amorphous Si layer recrystallizes via liquid-phase epitaxial growth with a solidification speed in the order of 10 m/s while cooling down [34]. After pulsed laser melting (PLM), the recrystallized layer is single-crystalline, free of extended defects, and doped with a Te concentration of around 1.5 at. % [12]. After PLM, all samples were cleaned by HF acid to remove the native SiO_2 layer and thereafter are referred as "as-fabricated" samples in this paper. Then the as-fabricated samples were individually subjected to thermal annealing in a furnace (Ströhlein Instruments, Germany). For the thermal stability analysis, isochronal anneals were performed covering a temperature range of 250–1200 °C for 10 min in a nitrogen atmosphere (purity: 99.99%).

B. Characterization

RBS/C was carried out to characterize the structural properties of samples before and after furnace annealing. The RBS/C measurements were performed using a 1-mm-diam collimated 1.7 MeV He^+ beam of the Rossendorf van de Graff accelerator with a 10–20 nA beam current. The backscattered particles were detected at an angle of 170° with respect to the incoming beam using silicon surface barrier detectors with an energy resolution of 15 keV. The channeling spectra were collected by aligning the sample to make the impinging He^+ beam parallel to the Si ⟨100⟩ axes. Also, angular axial scans around the ⟨100⟩ axis were measured using a two-axis goniometer. The integral backscattering yields in energy windows corresponding to scatterings from Si and Te atoms are then plotted as a function of the tilt angle. High-resolution TEM was performed on an image C_s-corrected Titan 80–300 microscope (FEI) operated at an accelerating voltage of 300 kV to analyze the microstructure of the samples before and after furnace annealing. To carry out qualitative chemical analysis, high-angle annular dark-field scanning transmission electron microscopy (HAADF-STEM) imaging and spectrum imaging based on energy-dispersive x-ray spectroscopy (EDXS) were done at 200 kV with a Talos F200X microscope equipped with an X-FEG electron source and a Super-X EDXS detector system (FEI). Prior to STEM analyses, the specimens mounted in a high-visibility low-background holder were placed for 10 s into a Model 1020 Plasma Cleaner (Fischione) to remove possible contamination. Classical cross-sectional TEM lamella preparation was done by sawing, grinding, polishing, dimpling, and final Ar ion milling.

The electrical properties of the Te-hyperdoped Si layers before and after subsequent furnace annealing were measured by a commercial Lakeshore Hall measurement system in the van der Pauw configuration [35] under a magnetic field perpendicular to the sample plane. The magnetic field was swept from −5 to 5 T. The gold electrodes were first sputtered onto the four corners of the squarelike samples. Prior to the sputtering process, the native SiO_2 layer was removed by etching in hydrofluoric acid (HF). Then, a silver conductive glue paste was applied to contact the wires to the gold electrodes. All contacts were confirmed to be ohmic by measuring the current-voltage curves at different temperatures.

The optical properties were investigated by Fourier transform infrared spectroscopy (FTIR) using a Bruker Vertex 80v FTIR spectrometer. In detail, transmittance (T) and reflectance (R) measurements were performed at room temperature with a KBr beam-splitter and a mid-IR DLaTGS detector in the infrared spectral range of 0.05–0.85 eV ($\lambda = 1.4-25\,\mu\mathrm{m}$). The sub-band-gap absorptance ($A = 1-T-R$) was then determined by recording the transmittance and reflectance spectra. A gold mirror was used as a 100% reflectance standard, and the illumination area of the spectrometer was focused on a spot diameter of about 3 mm to ensure that the measurements were performed solely within the sample area ($5 \times 5\,\mathrm{mm}^2$).

III. RESULTS AND DISCUSSION

A. Thermal stability of the structural properties

Figure 1(a) depicts the representative RBS spectra in a random/channeling configuration of Te-hyperdoped Si layers after furnace annealing. The reference channeling spectra of the as-implanted sample, the as-fabricated sample, and the bare silicon substrate are also included. As is well-established, χ_{min} (channeling minimum yield), which is defined as the ratio of the backscattering yield of the channeling to the random spectra, represents the degree of lattice damage in the host material. Consistent with previous works [12,36], the channeling spectrum of the as-implanted Te-hyperdoped Si layer shows a broad damage peak from 870 to 935 keV with a χ_{min} of 94%, which indicates that the as-implanted layer is completely damaged and amorphous. On the contrary, the backscattering yields in the channeling condition of the as-fabricated sample have a χ_{min} of 4% (from 800 to 910 keV), which points out that a high-quality single crystal has been restored after the PLM process [12]. Unexpectedly,

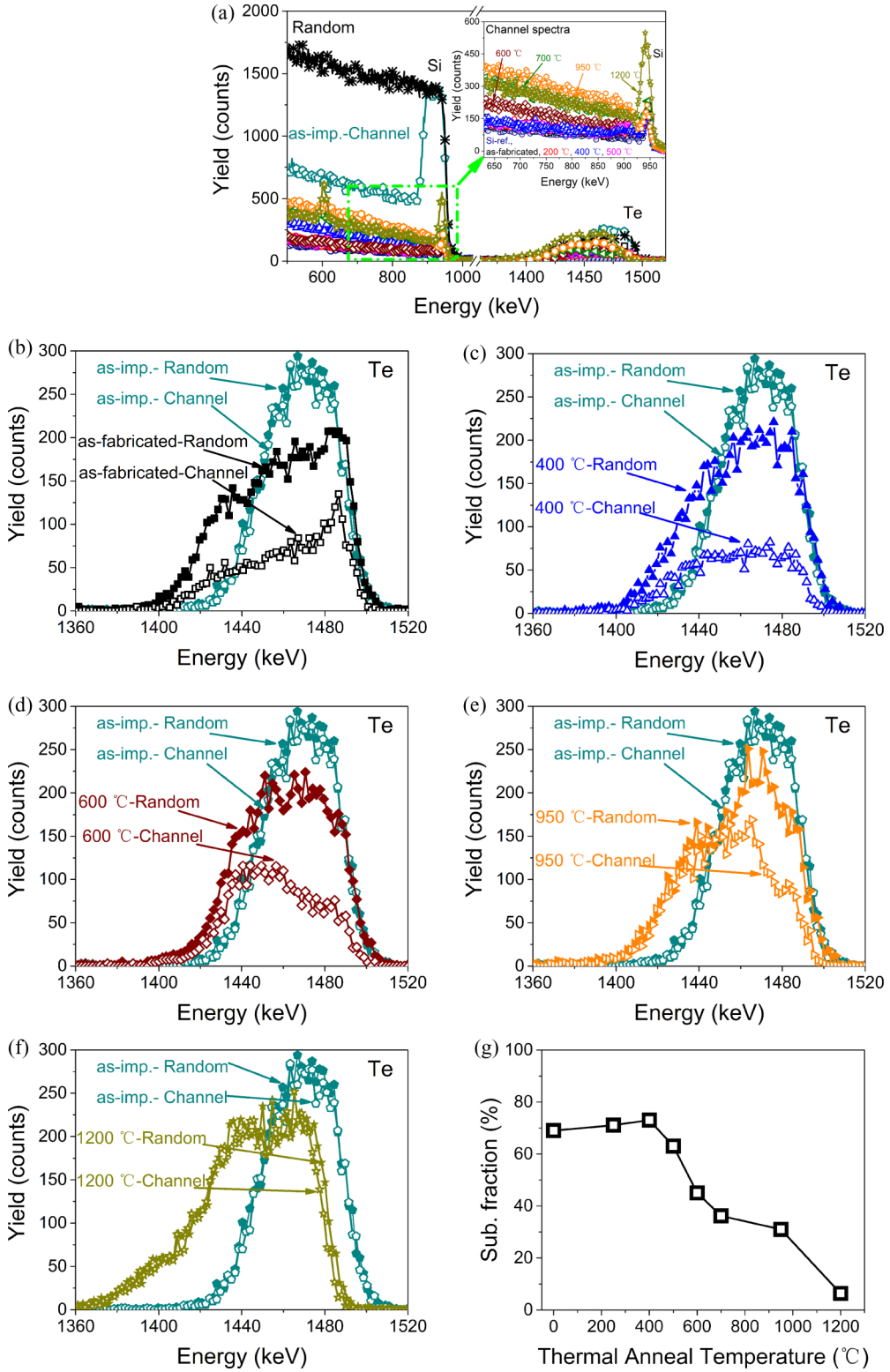

FIG. 1. (a) A sequence of RBS/C spectra of Te-hyperdoped Si layers furnace-annealed for 10 min at different temperatures (red: 250 °C; blue: 400 °C; magenta: 500 °C; wine: 600 °C; olive: 700 °C; orange: 950°C; dark yellow: 1200 °C). The channeling spectra of the as-fabricated sample (black) and the virgin Si (navy) are also included as references. The inset shows the magnification of Si signals from the channeling spectra. (b)–(f) The corresponding random and channeling Te profiles compared to the as-implanted Te distribution measured by RBS/C [(b) the as-fabricated sample, (c) 400 °C, (d) 600 °C, (e) 950 °C, and (f) 1200 °C]. (g) The Te substitutional fraction as a function of the furnace annealing temperature.

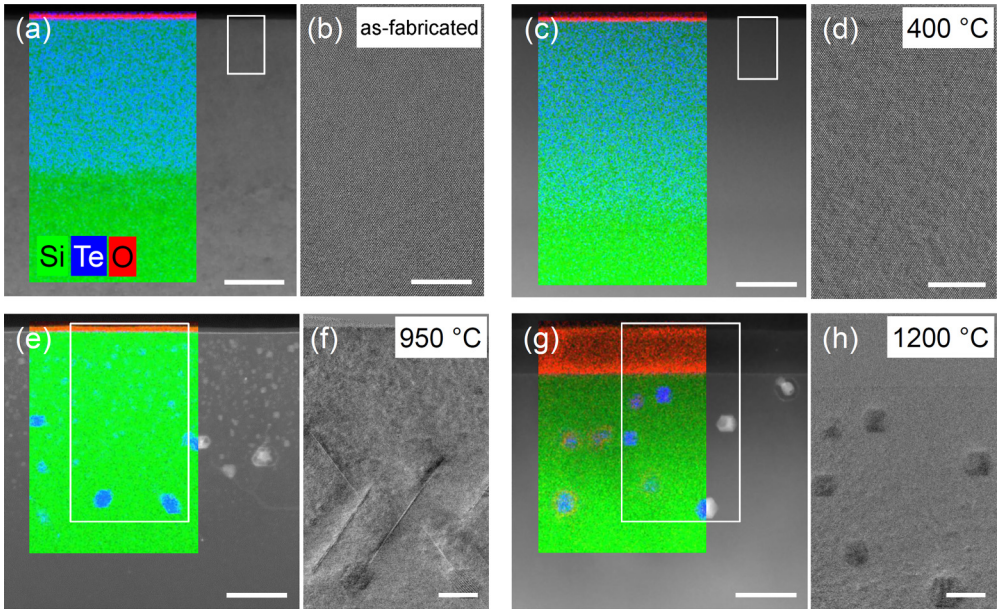

FIG. 2. Cross-sectional HAADF-STEM images superimposed with the corresponding EDXS element maps (blue: tellurium; green: silicon; red: oxygen) and representative HRTEM images for the field of view as depicted by the associated white rectangle for selected Te-hyperdoped Si layers. Parts (a) and (b) as-fabricated sample; (c) and (d) 400 °C; (e) and (f) 950 °C; and (g) and (h) 1200 °C. Scale bars: 50 nm for (a), (c), (e), and (g); 20 nm for (f) and (h); 10 nm for (b) and (d).

the crystalline quality of the furnace annealed samples with annealing temperatures below 500 °C remains good because the $\chi_{\min}$ values are comparable to that of the as-fabricated sample. However, for samples with a furnace annealing temperature above 500 °C, a clear increase of $\chi_{\min}$ was observed. This suggests an increased amount of disorder and a low crystalline quality in the Te-hyperdoped layer induced by high-temperature furnace annealing.

Figures 1(b)–1(f) show the RBS/C Te signal taken from both the random and channeling directions of the selected Te-hyperdoped Si layers juxtaposed with the corresponding spectra of the as-implanted layer. As shown in Figs. 1(b) and 1(c), upon annealing up to 400 °C the depth profile of Te is not significantly changed, but the channeling spectrum yield is reduced near the surface region (around 1490 keV). This proves that the Te dopants remain at the Si lattice sites and part of the interstitials are moved to the substitutional Si sites [37], particularly near the surface upon annealing up to 400 °C. However, the channeling effect becomes deteriorated starting from the deeper depth of the doped layer as the furnace annealing temperature increases, as shown in Figs. 1(d) and 1(e). Finally, the RBS random and channeling spectra of the Te signal are nearly overlapped in the 1200 °C sample [see Fig. 1(f)].

To gain a quantitative estimation, the Te substitutional fraction is approximated by

$$f_{\text{sub}} = \frac{1 - \chi_{\min}(\text{Te})}{1 - \chi_{\min}(\text{Si})}, \tag{1}$$

where f_{sub} is the fraction of impurity (Te) in the substitutional site, $\chi_{\min}(\text{Te})$ is the ratio of the channeling and random Te yield integrated over the recrystallization depth, and $\chi_{\min}(\text{Si})$ is the corresponding value for Si at the same depth along the [100] direction [37]. As shown in Fig. 1(g), the substitutional fraction of Te in furnace-annealed samples with annealing temperature up to 400 °C exhibits a slight increase. Afterward, it decreases as the temperature increases above 400 °C. Therefore, this suggests that the structural stability of the Te-hyperdoped Si layer can be preserved up to a postthermal anneal of 400 °C for 10 min.

Figure 2 shows representative HAADF-STEM images and corresponding HRTEM micrographs of selected Te-hyperdoped Si layers. For the as-fabricated sample, single-crystalline regrowth is confirmed by HRTEM imaging [Fig. 2(b), also described previously in Ref. [12]], while Te is distributed homogeneously within the top 120 nm [shown in Fig. 2(a)]. Furnace annealing at 400 °C does not change the microstructure, i.e., the epitaxial Te-hyperdoped layer is not affected [Fig. 2(d)]. The Te distribution is laterally homogeneous. In contrast to the as-fabricated sample, there is a rather smooth and gradual change of the Te density with depth [Fig. 2(c)].

However, first structural changes are observed in the sample annealed at 500 °C and are more pronounced for that annealed at 600 °C. As shown by the appearance of small bright dots in the HAADF-STEM images in Figs. 3(a) and 3(b), Te starts diffusing and tends to create small clusters at 500 and 600 °C, respectively. Hence, the annealing-related energy is high enough to induce the segregation of Te atoms. For both samples, the microstructure of the recrystallized layer remains single-crystalline (not shown here). At even higher furnace-annealing temperatures, such as 950 °C, Te can be found at defects/stacking faults, which indicates that the Si crystalline quality is no longer uniform. Additionally, the segregated Te clusters grow and form Te-rich secondary phase particles in the doped layer, which have a diameter on the order of 5 nm, some of them reaching a diameter of 20 nm [Figs. 2(e)

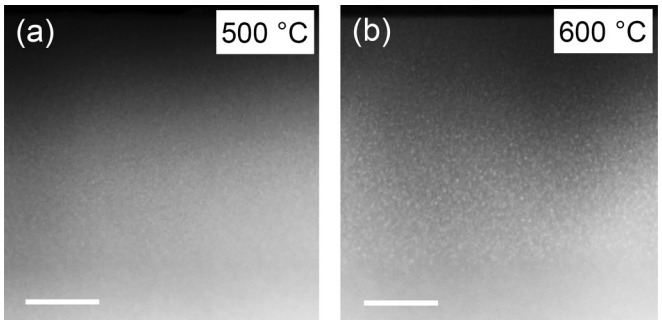

FIG. 3. Cross-sectional HAADF-STEM images for Te-hyperdoped Si layers after furnace treatment at 500 °C (a) and 600 °C (b) for 10 min., respectively. Scale bars: 50 nm.

and 2(f)]. These larger Te-rich clusters are mainly observed in the deeper region of the hyperdoped layer. This is in good agreement with the RBS/C data, where the channeling effect is no longer obvious particularly in the deeper region, and the Te substitutional fraction decreases significantly for the 950 °C sample. For the sample furnace-annealed at 1200 °C, the Te-rich clusters become larger and are distributed within the whole layer. Additionally, a 35-nm-thick silicon oxide surface layer is found to grow [Figs. 2(g) and 2(h)].

B. Evolution of the impurity lattice occupation with annealing

To unambiguously determine the effect of thermal annealing on the Te demixing with various furnace-annealing temperatures, RBS/C full angular scans about the [100] axes were performed. Figure 4 shows the angular distributions of the normalized yield of He ions backscattered by Te and Si at the same depth as a function of tilt angle for the furnace-annealed samples with different temperatures. The corresponding angular scan of the as-fabricated sample is also included as a reference. As described in Refs. [38,39], the two typical parameters $\chi_{\min}$ (the minimum value of the normalized yield in the angular scan, which is equivalent to the previous definition in Sec. III A) and $\psi_{1/2}$ (the half-width at half-maximum of the angular scans between $\chi_{\min}$ and 1) are used to characterize the angular distributions [38,39]. $\chi_{\min}$-Te is higher than $\chi_{\min}$-Si, and $\psi_{1/2}$-Te is narrower than $\psi_{1/2}$-Si, as shown in Fig. 4(a). As was well-established [38–40], the angular scan of Te will overlap with that of Si in the case of substitutional Te (Te_{Si}). A peak is expected to arise in the middle of the angular scan for interstitial Te ions. The angular scan of substitutional Te atoms but slightly displaced from the Si lattice is expected to be narrow and shallow. For furnace-annealing temperatures up to 400 °C, the majority of Te atoms are located on substitutional sites but with small displacement [see Fig. 4(c)], and a small amount of Te is at interstitial sites. As described in our previous work [36], the small displacement can be induced by the formation of Te_{Si}-vacancy-Te_{Si}, Te_{Si}-$Te_{interstitial}$ compensators, or Te_{Si}-Te_{Si} dimers, but the Te_{Si}-Te_{Si} dimers are more energetically favorable. At annealing temperatures higher than 400 °C, however, $\chi_{\min}$-Te gradually increases and $\psi_{1/2}$-Te gradually decreases, as shown in Figs. 4(d)–4(h). These results suggest that as the furnace annealing temperature increases, the majority of Te dopants gradually move out of the lattice positions into

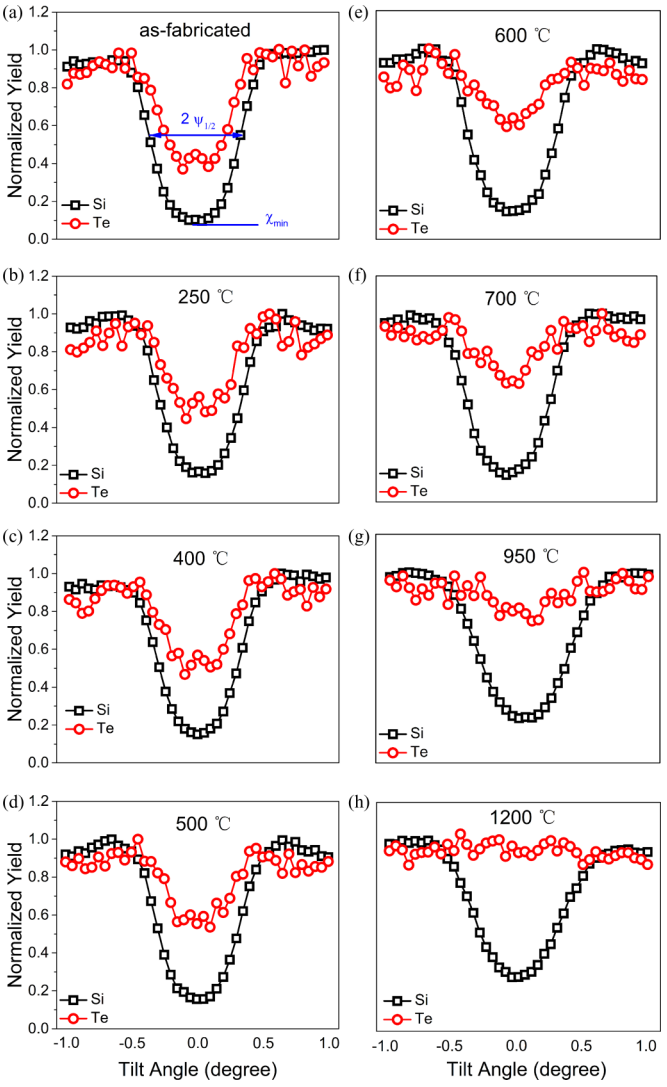

FIG. 4. Angular scans about the ⟨100⟩ axes for Te-hyperdoped Si samples of (a) the as-fabricated sample, and (b)–(h) samples with the same condition after furnace annealing with different temperatures for 10 min. Angular distributions have been normalized in a random direction. The red circle corresponds to Te atoms and the black square corresponds to Si. Solid lines are drawn through the symbols.

nonsubstitutional sites to form Te-V_m complexes (V_m denotes m Si vacancies, as reported in As-hyperdoped Si [41]), clusters, and even precipitates, which has been confirmed by the TEM results [see Figs. 2(e)–2(h)].

The angular scan results show the different lattice sites prevailing at different annealing temperatures, as a result of their thermal stabilities. From Fig. 1(g), one can identify at which temperature the substitutional fraction starts decreasing. Therefore, following the procedure of Arrhenius models for the thermally activated migration described in Refs. [42–44], the migration energy (E_M) of Te_{Si}-Te_{Si} can be obtained by

$$E_M = k_B T \ln\left[\frac{\nu_0 \Delta t}{N} \frac{1}{\ln\left(\frac{f_{n-1}}{f_n}\right)}\right], \tag{2}$$

where k_B is the Boltzmann constant, T is the furnace annealing temperature (here, $T = 500\,^{\circ}\mathrm{C}$ is applied in the calculation), Δt is the furnace annealing duration (in seconds), $\mathcal{V}_0$ is the attempt frequency, here using a typical value of $10^{12}\,\mathrm{s}^{-1}$, i.e., of the order of the lattice vibrations, f_{n-1} is the substitutional fraction before annealing at T, f_n is the fraction after the annealing at T, and N is the required number of steps before a substitutional Te atom moves off from the substitutional site into a random position. The estimation of the maximum and minimum E_M was described in detail in Refs. [42–44], where two opposite scenarios for the limit of the number of steps N before the movement of $\mathrm{Te_{Si}}$ were considered. The maximum E_M corresponds to the assumption that only one jump ($N = 1$) is considered enough to move a $\mathrm{Te_{Si}}$ atom out to a random position, while the minimum E_M is related to a reasonable assumption on the maximum number of jumps (N_max) that take place before the $\mathrm{Te_{Si}}$ atom is kicked out from the substitutional site into a random position. In the latter case, $N_\mathrm{max} \sim 2 \times 10^5$ by assuming that the diffusion length is comparable to the implantation depth [44]. Therefore, the resulting E_M is estimated to be between 2.3 eV (for $N = 1$) and 1.8 eV (for $N_\mathrm{max} \sim 2 \times 10^5$). Here, E_M of 2.3 eV is probably closer to the real situation since most vacancies will annihilate during annealing or form larger multiatom Te complexes. Therefore, a maximum migration energy is found to be $E_\mathrm{M} = 2.3\,\mathrm{eV}$, which is higher than that measured for S-hyperdoped Si, around 1.8 eV [29]. This indicates that Te-hyperdoped Si has a better thermal stability compared to S-hyperdoped Si.

C. Thermal stability of the electrical-transport properties

Electrical characterization has been performed to gain further insight into the electrical activation efficiency of the Te dopants in Si. To avoid the influence of the parallel conduction from the Si substrate, samples prepared on the *intrinsic* Si substrate ($\rho > 10^4\,\Omega\,\mathrm{cm}$) were measured. Figure 5(a) shows that the temperature-dependent sheet resistance (R_s) of furnace-annealed samples evolves with anneal temperature. The as-fabricated sample is also included as a reference. At room temperature, the R_s of the furnace-annealed samples is less than 600 Ω/square, which corresponds to a resistivity of less than $10^{-2}\,\Omega\,\mathrm{cm}$ (using the effective thickness of 120 nm). This confirms that the intrinsic Si substrate has no influence on the transport properties of the furnace annealed layers considering the respective thickness. R_s has a remarkably nonmonotonic evolution, which first decreases with increasing furnace-annealing temperature. However, the samples annealed at 950 and 1200 °C show a remarkable increase in resistance and change from metallic-like to semiconductor-like, as seen from the temperature-dependent resistance. Moreover, the free-electron concentration (n_s) and Hall mobility (μ) obtained from Hall measurements via the van der Pauw geometry [35] are plotted versus the furnace-annealing temperature in Fig. 5(b). As expected, n_s also exhibits a nonmonotonic evolution with annealing, which is of the same qualitative trend as R_s. In detail, n_s first increases by 27% (annealing temperature $\leqslant$400 °C) and then decreases to about 2% (1200 °C) of its initial value [see the black square in Fig. 5(b)]. Meanwhile, μ remains essentially constant at around $14\,\mathrm{cm}^2/\mathrm{V\,s}$ with

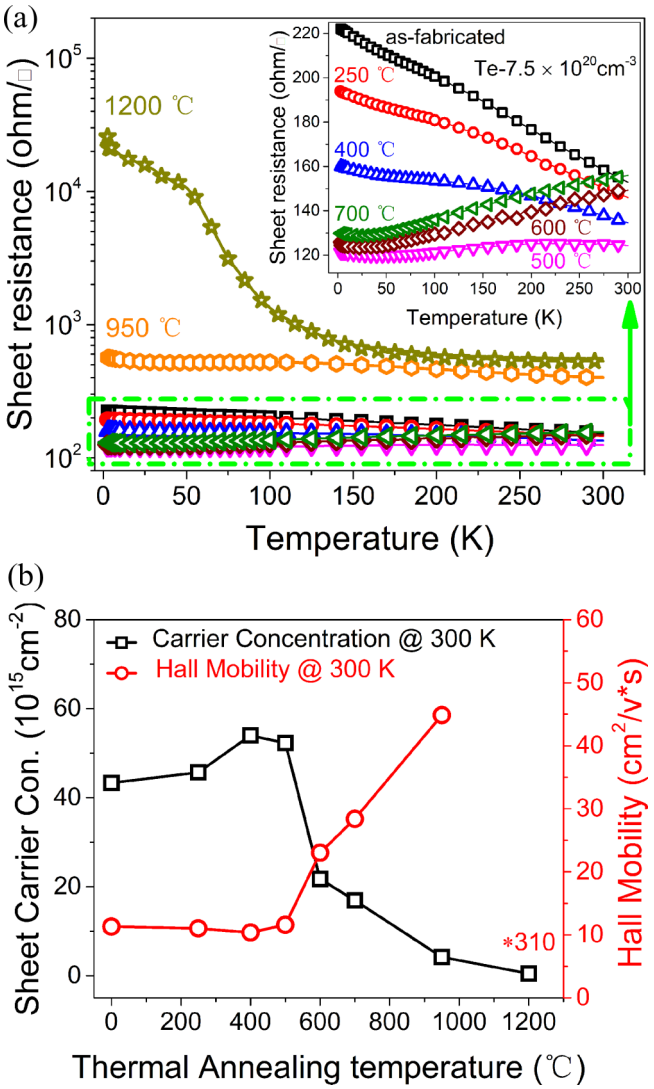

FIG. 5. Evolution of the electrical properties for the furnace-annealed Te-hyperdoped Si samples with an annealing duration of 10 min at different annealing temperatures. The annealing temperatures are indicated in the labels. The as-fabricated sample is also included as a reference. (a) Temperature-dependent sheet resistance R_s in the temperature range of 2–300 K. The inset shows the magnification of the data for samples with lower annealing temperatures. (b) Sheet carrier concentration n_s (black square) and Hall mobility μ (red circle) for each of the samples in (a). Solid lines drawn through the symbols are a guide for the eye.

annealing temperature $\leqslant$400°C and subsequently increases monotonically to $310\,\mathrm{cm}^2/\mathrm{V\,s}$ after annealing at 1200 °C.

The remarkable nonmonotonic evolution of electrical properties shown here is in agreement with the deactivation of S-hyperdoped Si reported in Ref. [33]. Here, a possible mechanistic interpretation is proposed to explain the nonmonotonic evolution. The initial electrical-active states are substitutional Te dopants (single $\mathrm{Te_{Si}}$ or $\mathrm{Te_{Si}}$-$\mathrm{Te_{Si}}$ dimers), which are the dominant states in Te-hyperdoped Si (verified by the RBS/C results). Then, after annealing at lower temperatures, the increase of n_s is attributed to the increase of the substitutional fraction of Te dopants [see Fig. 1(g)] and the decrease of

the residual disorder after the PLM process [45], while the unchanged μ is due to the dominant scattering of the ionized impurity. Particularly, the annealing between 500 and 700 °C presents an intermediate stage where n_s decreases but μ increases, leading to a smaller R_s. After annealing at even higher temperatures, electrically inactive complexes (e.g., vacancy-impurity complexes, clusters, or precipitates) tend to form. Moreover, the fraction of these inactivated states increases as the annealing temperature increases, which results in the eventual decrease of n_s.

D. Thermal stability of the sub-band-gap optical absorption

The evolution of the sub-band-gap absorptance as a function of furnace-annealing temperature was investigated to analyze the optical activity of the Te dopants in Si. Accompanying the formation of Te complexes (inactive centers) and the concomitant decrease in the substitutional fraction (as shown in Secs. III A and III B) at higher temperature anneals, the sub-band-gap optical absorptance is also expected to decrease. Figure 6(a) shows the optical absorptance for as-fabricated Te-hyperdoped Si samples subjected to furnace annealing at different temperatures. The as-fabricated sample and the bare Si substrate are also shown as a reference. The absorptance below 0.2 eV can be partially attributed to the free-carrier absorption [46]. Particularly, a strong and broad sub-band-gap optical absorptance (from 0.20 to 0.87 eV) is observed in the as-fabricated sample and in the furnace-annealed samples while the reference silicon substrate has no such absorptance. This is consistent with the previous reported works [12]: the well-defined broad absorptance band comes from the presence of a Te-mediated impurity band (IB) in the upper half of the Si band gap. As shown in Fig. 6(a), the sub-band-gap optical absorptance in the Te-hyperdoped Si presents a pronounced nonmonotonic evolution with furnace annealing. The strongest broadband absorptance is found to take place when a postfurnace annealing at 400 °C for 10 min is applied.

To quantify the sub-band-gap absorptance for each sample, the strength of the optical absorption is defined as the integral of the absorptance spectrum from 0.20 to 0.87 eV [12,46]. Figure 6(b) shows the integrated sub-band-gap absorptance (A_{int}) as a function of furnace-annealing temperature, where the as-fabricated sample presents an A_{int} of 0.31 as the initial value. A_{int} first increases by 21% with increasing annealing temperature up to 400 °C and then gradually decreases to about 0.072 by 78% of its initial value if the annealing temperature increases up to 1200 °C [see Fig. 6(b)]. The enhancement of A_{int} for samples annealed at 250 and 400 °C not only corresponds to the increase of the substitutional Te, but it can also be partially attributed to the removal of the lattice distortion and the residual disorder after the prior pulsed laser melting process [45]. The apparent reduction of A_{int} with the furnace annealing temperature increasing from 500 to 1200 °C is related to the change in the metastable atomic configuration of Te atoms in the Si matrix, which is confirmed by the RBS results. The nonmonotonic evolution of A_{int} with the thermal anneals is consistent with the variation of the substitutional Te fraction.

Figure 6(c) displays the integrated sub-band-gap absorptance as a function of substitutional Te concentration.

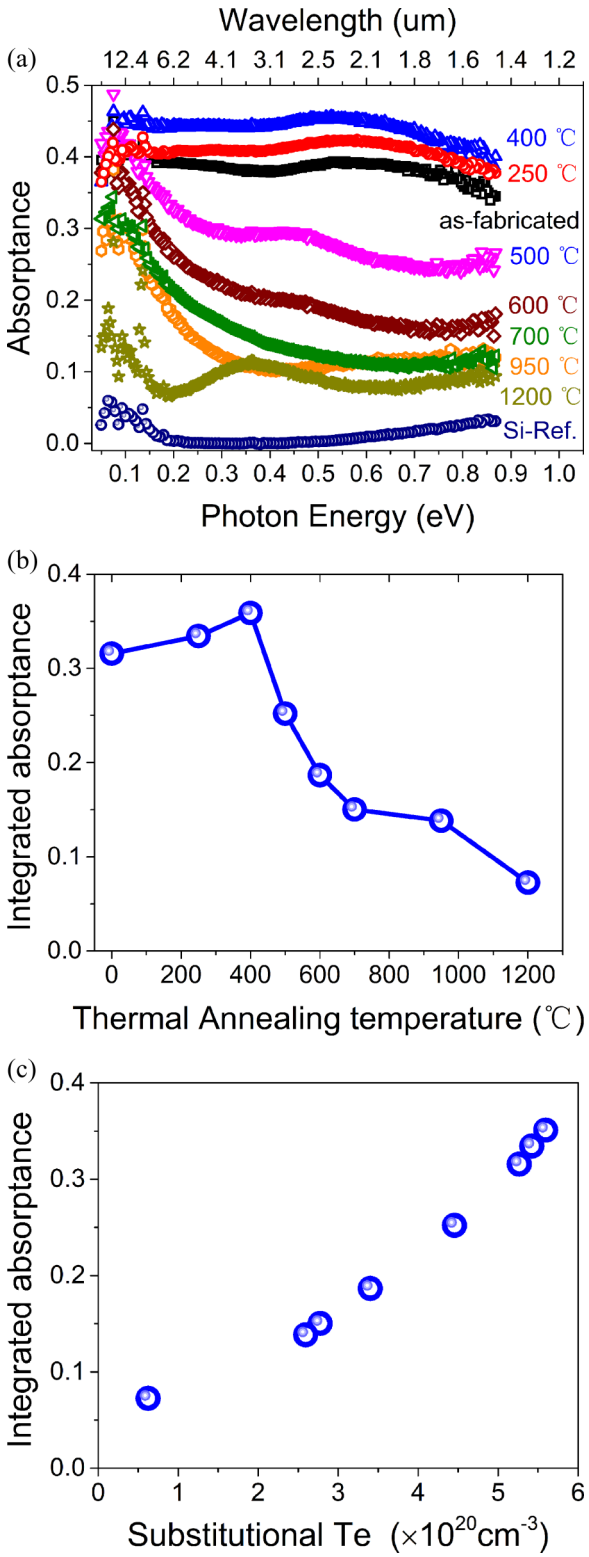

FIG. 6. (a) Sub-band-gap absorptance of as-fabricated Te-hyperdoped Si samples with an annealing duration of 10 min at different temperatures. The annealed temperatures are indicated as labels. The reference absorptance of an as-fabricated sample and the pure Si substrate is also included. (b) Integrated absorptance (A_{int}) from 0.20 to 0.87 eV of the furnace-annealed samples as a function of annealing temperature. (c) A_{int} of the as-fabricated sample and furnace-annealed samples as a function of substitutional Te concentration (determined by RBS/C).

A direct correlation is observed between A_{int} and the total substitutional Te concentration. Such a strong correlation indicates that the electronic states introduced by substitutional Te are the origin of the sub-band-gap absorptance in hyperdoped Si. This is in strong agreement with the previous work reported in Refs. [32] and [46], where the thermal anneals were also found to result in the deactivation of optical-active centers responsible for the sub-band-gap absorptance [29,46]. However, the Te-hyperdoped Si system exhibits a thermal stability and tolerates annealing up to 400 °C, which is promising for the integration of CMOS-compatible optoelectronics.

IV. CONCLUSION

We have examined the thermal stability of Te-hyperdoped Si subjected to isochronal anneals from 250 to 1200 °C. We have demonstrated that the recrystallization quality, the Te substitutionality, the electrical activation, and the room-temperature sub-band-gap absorption do not exhibit substantial changes upon furnace annealing at temperatures of 400 °C for 10 min. Instead, an impairment of the structural, electrical, and optical properties is found as the annealing temperature increases above 400 °C. We have proven that the Te-hyperdoped Si layer possesses a thermal stability that is crucial for the realization of CMOS-compatible devices. In particular, we have found that the electrical and optical deactivation caused by the thermal treatment is attributed to the thermally activated atomic-scale migration of Te dopants with a maximum migration energy of 2.3 eV. At the atomic scale we have established a one-to-one correlation between the substitutional Te dopants and the unique properties. The knowledge of Te dopant transformation caused by thermal treatment contributes to achieving optimal properties such as an extremely high carrier concentration and strong sub-band-gap absorption for Si-based micro-/optoelectronics.

ACKNOWLEDGMENTS

The authors acknowledge the Ion Beam Center (IBC) at Helmholtz-Zentrum Dresden-Rossendorf (HZDR) for performing the Te implantations. M.W. thanks I. Skorupa for her assistance in furnace annealing. Furthermore, the authors acknowledge R. Aniol for TEM specimen preparation. Additionally, support by the Structural Characterization Facilities at IBC and funding of TEM Talos by the German Federal Ministry of Education of Research (BMBF), Grant No. 03SF0451 in the framework of HEMCP are gratefully acknowledged. This work is funded by the Helmholtz-Gemeinschaft Deutscher Forschungszentren (HGF-VH-NG-713). M.W. gratefully acknowledges financial support by the Chinese Scholarship Council (File No. 201506240060). Y.B. would like to thank the Alexander–von Humboldt Foundation for providing a postdoctoral fellowship.

[1] C. White, S. Wilson, B. Appleton, and F. Young, Jr., Supersaturated substitutional alloys formed by ion implantation and pulsed laser annealing of group-III and group-V dopants in silicon, J. Appl. Phys. **51**, 738 (1980).

[2] C. White, J. Narayan, and R. Young, Laser annealing of ion-implanted semiconductors, Science **204**, 461 (1979).

[3] C. White, P. Pronko, S. Wilson, B. Appleton, J. Narayan, and R. Young, Effects of pulsed ruby-laser annealing on As and Sb implanted silicon, J. Appl. Phys. **50**, 3261 (1979).

[4] P. W. Chapman, O. N. Tufte, J. D. Zook, and D. Long, Electrical properties of heavily doped silicon, J. Appl. Phys. **34**, 3291 (1963).

[5] P. Dai, Y. Zhang, and M. Sarachik, Electrical conductivity of metallic Si: B near the metal-insulator transition, Phys. Rev. B **45**, 3984 (1992).

[6] A. J. Said, D. Recht, J. T. Sullivan, J. M. Warrender, T. Buonassisi, P. D. Persans, and M. J. Aziz, Extended infrared photoresponse and gain in chalcogen-supersaturated silicon photodiodes, Appl. Phys. Lett. **99**, 073503 (2011).

[7] S. Hu, P. Han, S. Wang, X. Mao, X. Li, and L. Gao, Structural and optoelectronic properties of selenium-doped silicon formed using picosecond pulsed laser mixing, Phys. Status Solidi A **209**, 2521 (2012).

[8] E. Garcia-Hemme, R. Garcia-Hernansanz, J. Olea, D. Pastor, A. del Prado, I. Martil, and G. Gonzalez-Diaz, Sub-bandgap spectral photo-response analysis of Ti supersaturated Si, Appl. Phys. Lett. **101**, 192101 (2012).

[9] J. P. Mailoa, A. J. Akey, C. B. Simmons, D. Hutchinson, J. Mathews, J. T. Sullivan, D. Recht, M. T. Winkler, J. S. Williams, J. M. Warrender, P. D. Persans, M. J. Aziz, and T. Buonassisi, Room-temperature sub-band gap optoelectronic response of hyperdoped silicon, Nat. Commun. **5**, 3011 (2014).

[10] X. Qiu, X. Yu, S. Yuan, Y. Gao, X. Liu, Y. Xu, and D. Yang, Trap assisted bulk silicon photodetector with high photoconductive gain, low noise, and fast response by Ag hyperdoping, Adv. Opt. Mater. **6**, 1700638 (2018).

[11] Y. Berencén, S. Prucnal, F. Liu, I. Skorupa, R. Hubner, L. Rebohle, S. Zhou, H. Schneider, M. Helm, and W. Skorupa, Room-temperature short-wavelength infrared Si photodetector, Sci. Rep. **7**, 43688 (2017).

[12] M. Wang, Y. Berencén, E. García-Hemme, S. Prucnal, R. Hübner, Y. Yuan, C. Xu, L. Rebohle, R. Böttger, and R. Heller, Extended infrared photoresponse in Te-hyperdoped Si at room temperature, Phys. Rev. Appl. **10**, 024054 (2018).

[13] B. K. Newman, M.-J. Sher, E. Mazur, and T. Buonassisi, Reactivation of sub-bandgap absorption in chalcogen-hyperdoped silicon, Appl. Phys. Lett. **98**, 251905 (2011).

[14] M.-J. Sher, Y.-T. Lin, M. T. Winkler, E. Mazur, C. Pruner, and A. Asenbaum, Mid-infrared absorptance of silicon hyperdoped with chalcogen via fs-laser irradiation, J. Appl. Phys. **113**, 063520 (2013).

[15] A. Martí, E. Antolín, P. Linares, E. Cánovas, D. F. Marrón, C. Tablero, M. Mendes, A. Mellor, I. Tobías, and M. Levy, *34th IEEE Photovoltaic Specialists Conference* (IEEE, Piscataway, NJ, 2009), p. 002486.

[16] C. H. Crouch, J. E. Carey, M. Shen, E. Mazur, and F. Y. Genin, Infrared absorption by sulfur-doped silicon formed by femtosecond laser irradiation, Appl. Phys. A **79**, 1635 (2004).

[17] X. Dong, N. Li, Z. Zhu, H. Shao, X. Rong, C. Liang, H. Sun, G. Feng, L. Zhao, and J. Zhuang, A nitrogen-hyperdoped silicon material formed by femtosecond laser irradiation, Appl. Phys. Lett. **104**, 091907 (2014).

[18] J. T. Sullivan, C. B. Simmons, T. Buonassisi, and J. J. Krich, Targeted search for effective intermediate band solar cell materials, IEEE J. Phot. **5**, 212 (2015).

[19] P. D. Persans, N. E. Berry, D. Recht, D. Hutchinson, H. Peterson, J. Clark, S. Charnvanichborikarn, J. S. Williams, A. DiFranzo, M. J. Aziz, and J. M. Warrender, Photocarrier lifetime and transport in silicon supersaturated with sulfur, Appl. Phys. Lett. **101**, 111105 (2012).

[20] E. Antolín, A. Martí, J. Olea, D. Pastor, G. González-Díaz, I. Mártil, and A. Luque, Lifetime recovery in ultrahighly titanium-doped silicon for the implementation of an intermediate band material, Appl. Phys. Lett. **94**, 042115 (2009).

[21] M. N. Alexander and D. F. Holcomb, Semiconductor-to-metal transition in n-type group IV semiconductors, Rev. Mod. Phys. **40**, 815 (1968).

[22] E. Ertekin, M. T. Winkler, D. Recht, A. J. Said, M. J. Aziz, T. Buonassisi, and J. C. Grossman, Insulator-to-Metal Transition in Selenium-Hyperdoped Silicon: Observation and Origin, Phys. Rev. Lett. **108**, 026401 (2012).

[23] M. T. Winkler, D. Recht, M. J. Sher, A. J. Said, E. Mazur, and M. J. Aziz, Insulator-to-Metal Transition in Sulfur-Doped Silicon, Phys. Rev. Lett. **106**, 178701 (2011).

[24] D. Pastor, J. Olea, A. del Prado, E. García-Hemme, I. Mártil, and G. González-Díaz, *Spanish Conference on Electron Devices* (IEEE, Piscataway, NJ, 2011), p. 1.

[25] E. García-Hemme, D. Montero, R. García-Hernansanz, J. Olea, I. Mártil, and G. González-Díaz, Insulator-to-metal transition in vanadium supersaturated silicon: Variable-range hopping and Kondo effect signatures, J. Phys. D **49**, 275103 (2016).

[26] K. C. Pandey, A. Erbil, I. G. Cargill, R. F. Boehme, and D. Vanderbilt, Annealing of Heavily Arsenic-Doped Silicon: Electrical Deactivation and a New Defect Complex, Phys. Rev. Lett. **61**, 1282 (1988).

[27] P. M. Rousseau, P. B. Griffin, W. T. Fang, and J. D. Plummer, Arsenic deactivation enhanced diffusion: A time, temperature, and concentration study, J. Appl. Phys. **84**, 3593 (1998).

[28] Y. Takamura, A. Vailionis, A. F. Marshall, P. B. Griffin, and J. D. Plummer, Dopant deactivation in heavily Sb doped Si (001): A high-resolution x-ray diffraction and transmission electron microscopy study, J. Appl. Phys. **92**, 5503 (2002).

[29] C. B. Simmons, A. J. Akey, J. J. Krich, J. T. Sullivan, D. Recht, M. J. Aziz, and T. Buonassisi, Deactivation of metastable single-crystal silicon hyperdoped with sulfur, J. Appl. Phys. **114**, 243514 (2013).

[30] R.-D. Chang and C.-H. Lin, Activation and deactivation of phosphorus in silicon-on-insulator substrates, Mater. Sci. Semicond. Proc. **42**, 219 (2016).

[31] B. K. Newman, E. Ertekin, J. T. Sullivan, M. T. Winkler, M. A. Marcus, S. C. Fakra, M.-J. Sher, E. Mazur, J. C. Grossman, and T. Buonassisi, Extended x-ray absorption fine structure spectroscopy of selenium-hyperdoped silicon, J. Appl. Phys. **114**, 133507 (2013).

[32] W. J. Min, K. Park, K.-S. Yu, S. Joo, Y.-S. Kim, and D. W. Moon, Identification of donor deactivation centers in heavily As-doped Si using time-of-flight medium-energy ion scattering spectroscopy, J. Appl. Phys. **118**, 135706 (2015).

[33] M. V. Limaye, S. C. Chen, C. Y. Lee, L. Y. Chen, S. B. Singh, Y. C. Shao, Y. F. Wang, S. H. Hsieh, H. C. Hsueh, J. W. Chiou, C. H. Chen, L. Y. Jang, C. L. Cheng, W. F. Pong, and Y. F. Hu, Understanding of sub-band gap absorption of femtosecond-laser sulfur hyperdoped silicon using synchrotron-based techniques, Sci. Rep. **5**, 11466 (2015).

[34] F. Spaepen, D. Turnbull, J. Poate, and J. Mayer, *Laser Annealing of Semiconductors* (Academic, New York, 1982).

[35] L. Van der Pauw, A method of measuring the resistivity and Hall coefficient on lamellae of arbitrary shape, Philips Tech. Rev. **20**, 320 (1958).

[36] M. Wang, A. Debernardi, Y. Berencén, R. Heller, C. Xu, Y. Yuan, Y. Xie, R. Böttger, L. Rebohle, and W. Skorupa, Breaking the doping limit in silicon by deep impurities, arXiv:1809.06055 [Phys. Rev. Appl. (to be published)].

[37] L. C. Feldman, J. W. Mayer, and S. T. Picraux, *Materials Analysis by Ion Channeling: Submicron Crystallography* (Academic, New York, 2012).

[38] C. Brizard, J. R. Regnard, J. L. Allain, A. Bourret, M. Dubus, A. Armigliato, and A. Parisini, Backscattering spectrometry and ion channeling studies of heavily implanted As+ in silicon, J. Appl. Phys. **75**, 126 (1994).

[39] L. C. Feldman, J. W. Mayer, and S. T. Picraux, *Materials Analysis by Ion Channeling* (Academic, New York, 1982).

[40] J. R. Tesmer and M. Nastasi, *Handbook of Modern Ion Beam Materials Analysis* (Materials Research Society, Pittsburgh, 1995).

[41] V. Ranki, K. Saarinen, J. Fage-Pedersen, J. L. Hansen, and A. N. Larsen, Electrical deactivation by vacancy-impurity complexes in highly As-doped Si, Phys. Rev. B **67**, 041201 (2003).

[42] D. J. Silva, U. Wahl, J. G. Correia, L. M. C. Pereira, L. M. Amorim, M. R. da Silva, E. Bosne, and J. P. Araújo, Lattice location and thermal stability of implanted nickel in silicon studied by on-line emission channeling, J. Appl. Phys. **115**, 023504 (2014).

[43] U. Wahl, A. Vantomme, G. Langouche, and J. G. Correia, Lattice Location and Stability of Ion Implanted Cu in Si, Phys. Rev. Lett. **84**, 1495 (2000).

[44] L. M. C. Pereira, U. Wahl, S. Decoster, J. G. Correia, M. R. da Silva, A. Vantomme, and J. P. Araújo, Direct identification of interstitial Mn in heavily p-type doped GaAs and evidence of its high thermal stability, Appl. Phys. Lett. **98**, 201905 (2011).

[45] W. Yang, A. J. Akey, L. A. Smillie, J. P. Mailoa, B. C. Johnson, J. C. McCallum, D. Macdonald, T. Buonassisi, M. J. Aziz, and J. S. Williams, Au-rich filamentary behavior and associated subband gap optical absorption in hyperdoped Si, Phys. Rev. Mater. **1**, 074602 (2017).

[46] I. Umezu, J. M. Warrender, S. Charnvanichborikarn, A. Kohno, J. S. Williams, M. Tabbal, D. G. Papazoglou, X.-C. Zhang, and M. J. Aziz, Emergence of very broad infrared absorption band by hyperdoping of silicon with chalcogens, J. Appl. Phys. **113**, 213501 (2013).